

Conditional Diffusion Models for Semantic 3D Medical Image Synthesis

Zolnamar Dorjsembe, Hsing-Kuo Pao, Sodtavilan Odonchimed, Furen Xiao

Abstract—The demand for artificial intelligence (AI) in healthcare is rapidly increasing. However, significant challenges arise from data scarcity and privacy concerns, particularly in medical imaging. While existing generative models have achieved success in image synthesis and image-to-image translation tasks, there remains a gap in the generation of 3D semantic medical images. To address this gap, we introduce Med-DDPM, a diffusion model specifically designed for semantic 3D medical image synthesis, effectively tackling data scarcity and privacy issues. The novelty of Med-DDPM lies in its incorporation of semantic conditioning, enabling precise control during the image generation process. Our model outperforms Generative Adversarial Networks (GANs) in terms of stability and performance, generating diverse and anatomically coherent images with high visual fidelity. Comparative analysis against state-of-the-art augmentation techniques demonstrates that Med-DDPM produces comparable results, highlighting its potential as a data augmentation tool for enhancing model accuracy. In conclusion, Med-DDPM pioneers 3D semantic medical image synthesis by delivering high-quality and anatomically coherent images. Furthermore, the integration of semantic conditioning with Med-DDPM holds promise for image anonymization in the field of biomedical imaging, showcasing the capabilities of the model in addressing challenges related to data scarcity and privacy concerns. Our code and model weights are publicly accessible on our GitHub repository at <https://github.com/mobaidoctor/med-ddpm/>, facilitating reproducibility.

Index Terms—Conditional diffusion models, semantic 3D image synthesis, generative models, anonymization, data augmentation

I. INTRODUCTION

DEEP learning has made remarkable progress in the medical field [1]–[3]. However, it encounters challenges due to the scarcity, heterogeneity, cost of annotation, and privacy concerns associated with medical data [4]–[7]. To overcome

"This work was supported by the National Science and Technology Council, Taiwan [Grant No. 111-2221-E-002-049-MY3] and National Taiwan University Hospital [Grant No. 110-EDN03]." (Corresponding author: Furen Xiao.)

Z. Dorjsembe and H. Pao are with the Department of Computer Science and Information Engineering, National Taiwan University of Science and Technology, Taipei 106, Taiwan (e-mail: d11115806@mail.ntust.edu.tw, pao@mail.ntust.edu.tw).

S. Odonchimed is with the Faculty of Engineering, The University of Tokyo, Tokyo 113-8654, Japan (e-mail: 1184142454@g.ecc.u-tokyo.ac.jp).

F. Xiao is with Institute of Medical Device and Imaging, National Taiwan University, College of Medicine, Taipei 100, Taiwan (e-mail: fxiao@ntu.edu.tw).

these challenges, generative models have emerged as a promising solution [8], [9], particularly in medical imaging [10]. These models offer valuable capabilities for data augmentation [11], image reconstruction [12], and privacy-preserving data anonymization [13], [14].

Semantic image synthesis enables precise control over unconditional image generation, allowing guidance and customization of the generated content. In the field of medical imaging, this capability holds significant potential, particularly in the synthesis of pathological images, where precise control over generative models is crucial, including the ability to position abnormal areas in specified locations.

While generative adversarial networks (GANs) are widely used in semantic image synthesis [15]–[17], they face challenges such as unstable training, mode collapse, and diminished gradient [18]. Moreover, many GAN techniques primarily focus on two-dimensional (2D) images, which is inadequate for the three-dimensional (3D) data requirements of medical imaging [19], [20].

Diffusion models have recently emerged as a leading approach in generative modeling, achieving state-of-the-art results in generating high-quality, realistic images [21], [22]. This has led to a growing interest in exploring their potential applications in the field of medical imaging [23]. However, despite recent advances, there remains a noticeable research gap in the exploration of semantic 3D medical image synthesis, with a predominant focus on 2D image synthesis.

In our previous work [24], we compared diffusion models with GAN models and discovered that diffusion models outperformed GAN models in unconditional 3D medical image synthesis. Building on these findings and with the intention of addressing the existing research gap, this study aims to enhance the capabilities of Denoising Diffusion Probabilistic Models (DDPMs) [25] by tackling the challenges posed by limited annotated datasets and privacy-preserving AI.

We propose a novel method, Med-DDPM, which incorporates segmentation masks into the diffusion process for pixel-level controllable 3D medical image synthesis. Our approach enables the generation of high-resolution, semantically guided 3D medical images and holds potential for extension to diverse image-to-image translation tasks within the medical domain.

To validate our approach, we conducted experiments using raw clinical brain MRI data without skull stripping. Specifically, we evaluated our proposed method using a limited number of images as a toy dataset and examined the impact of the synthesized images on the performance of a 3D U-Net

segmentation model [26]. The results illustrate the superiority of our approach compared to GAN-based methods, showcasing a wide diversity of generated images and achieving results that closely align with state-of-the-art augmentations in the segmentation task. Our proposed Med-DDPM demonstrates its remarkable effectiveness even with a small number of training images.

Furthermore, we conducted an additional experiment to validate the effectiveness of Med-DDPM, utilizing the brain-extracted MRI dataset from the BraTS2021 challenge¹. This experiment serves to showcase the remarkable capability of our proposed method in simultaneously generating all four modalities of MRI (T1, T1CE, T2, and Flair) from a segmentation mask.

Our contributions include: (1) Introducing Med-DDPM, a conditional diffusion model that utilizes pixel-level mask images for high-resolution 3D medical image synthesis. (2) Presenting empirical evidence that demonstrates the efficacy of Med-DDPM in enhancing segmentation model performance and serving as an alternative to data augmentation. (3) Offering mask conditioning synthesis, enabling the generation of both normal and pathological whole head MRIs of any size based on given masks. Experimental results showcase the generation of diverse and high-quality images, suggesting the potential for Med-DDPM to serve as an advanced data anonymization tool with further refinements. (4) Providing a publicly available synthetic dataset comprising brain pathological MR images with corresponding segmentation masks ([doi: 10.21227/3ej9-e459](https://doi.org/10.21227/3ej9-e459)), alongside accessible code and model weights on our GitHub repository at <https://github.com/mobaidoctor/med-ddpm/>.

In summary, this research introduces a novel approach to semantic 3D medical image synthesis, emphasizing the potential of diffusion models in addressing challenges related to data scarcity and privacy preservation in the field of medical imaging.

A. Related Work

Diffusion models have emerged as an area of interest since the publication of Denoising Diffusion Probabilistic Model (DDPM) [25] in 2020. However, compared to Generative Adversarial Networks (GANs), there are relatively few studies in this field. Existing papers primarily focus on 2D image synthesis [22], [27]. Diffusion models have demonstrated superior mode coverage and the ability to generate high-quality samples [28], making them appealing for medical image synthesis. Throughout the course of this study, several research papers focusing on medical image synthesis using diffusion models have been published in the literature [29]–[31]. A summary of publications related to diffusion models in the field of medical image analysis is provided by [32]. The summary reveals that all of these papers were recently published, indicating that this research direction is relatively new and requires further exploration. However, while these studies propose diffusion models for various purposes in medical image analysis, the majority of them are limited to

2D images and lack conditional methods, specifically pixel label conditioning, for 3D medical image synthesis. Given the established performance of diffusion models in medical image synthesis, there is a need for further exploration in diverse medical image analysis tasks.

II. METHOD

In this study, we extend our previous work on 3D-DDPM [24], which adapted the vanilla DDPM model for generating 3D volumetric images. We further enhance this architecture to facilitate the synthesis of conditional 3D medical images, conditioned on segmentation masks. Initially, our approach was grounded on the original DDPM, as proposed in [25]. The forward diffusion process q adds small quantities of Gaussian noise $\epsilon \sim \mathcal{N}(0, \mathbf{I})$, defined by the variance schedule $\bar{\alpha}_t$, to an image sample x_0 from the training dataset at each timestep t within a given number of timesteps T . The noisy sample x_t is defined as follows for $1 < t \leq T$:

$$x_t = \sqrt{\bar{\alpha}_t} x_0 + \sqrt{1 - \bar{\alpha}_t} \epsilon. \quad (1)$$

To prevent sudden noise level fluctuations, we adopt a cosine noise schedule, as defined in [33]:

$$\bar{\alpha}_t = \frac{f(t)}{f(0)}, \quad f(t) = \cos\left(\frac{t/T + s}{1+s} \cdot \frac{\pi}{2}\right)^2, \quad (2)$$

Here, parameter s is a small offset value that prevents the schedule from becoming exceedingly small as the timestep nears zero. As a denoiser model in the reverse diffusion process p_θ , we employ a modified 3D U-Net architecture, based on the original work [25] by DDPM authors. Our enhancements involve replacing 2D operations, layers, and noise inputs with 3D counterparts to handle volumetric medical images. We incorporate embedding, ResBlocks, SiLU activation, group normalization, attention and fully connected layers to enhance performance. The detailed architecture is illustrated in Fig. 1.

For model conditioning, we propose a straightforward, effective method that modifies the input image x_t by channel-wise concatenating the segmentation mask. Contrary to the original DDPM where x_t is the only input, our model \tilde{x}_t includes an additional channel for a segmentation mask. This mask guides the generation process, enabling the synthesis of meaningful images, such as a pathological MRI of the brain with a tumor precisely positioned. The conditioning process is illustrated in Fig. 1, where the segmentation mask c is concatenated with the noisy image x_t at each timestep t .

The training images and segmentation masks used in this study are single-channel volumetric images with three dimensions: width (w), height (h), and depth (d). The segmentation mask in the dataset consists of three class labels: 0 represents the background, 1 corresponds to the head area, and 2 indicates the tumor area. To align the mask image with the class labels, we performed a one-hot encoding operation, excluding the background class label 0 as it is not relevant. This operation resulted in a mask image with two channels, where channel 0 represented the head area and channel 1 indicated the tumor area. The channel-wise concatenation was then applied to

¹<http://braintumorsegmentation.org/>

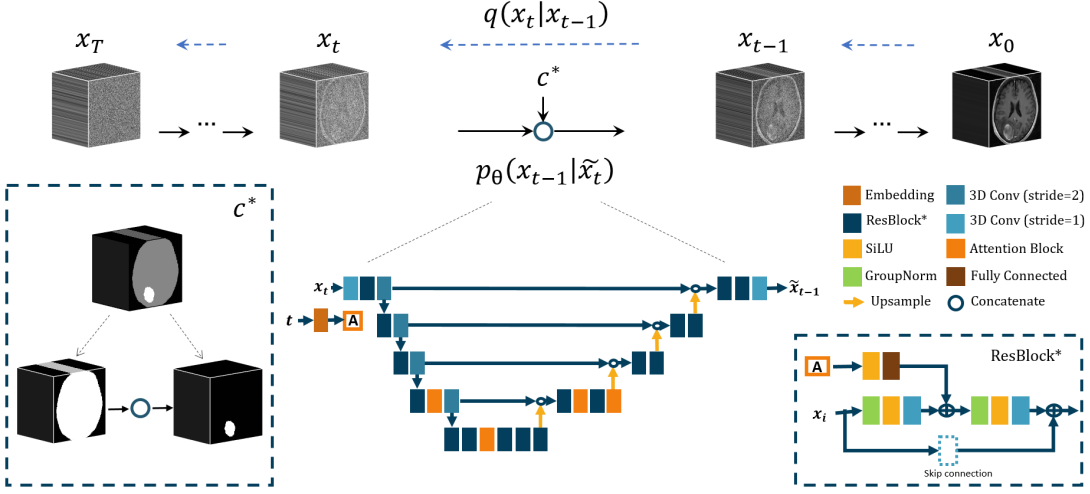


Fig. 1. Main architecture of the proposed method. The condition image, denoted as c^* , represents the one-hot encoded mask image. The building blocks of the noise predictor U-Net model, responsible for the $p_\theta(x_{t-1}|\tilde{x}_t)$ denoising process, are illustrated in detail.

combine the image and the mask, resulting in a concatenated image with three channels denoted as $\tilde{x}_t^{(3,w,d,h)} := x_t^{(1,w,d,h)} \oplus c^{2,w,d,h}$. Throughout this paper, we refer to the concatenated image as \tilde{x}_t .

The denoising process, also known as the generative sampling process, $x_{t-1} \sim p_\theta(x_{t-1}|x_t)$, is formulated as follows:

$$x_{t-1} = \frac{1}{\sqrt{\alpha_t}} \left(x_t - \frac{1 - \alpha_t}{\sqrt{1 - \bar{\alpha}_t}} \epsilon_\theta(\tilde{x}_t, t) \right) + \sigma_t z, \quad (3)$$

where $z \sim \mathcal{N}(0, \mathbf{I})$, $\sigma_t = \sqrt{\beta_t}$, $\beta_t \in (0, 1)$, ϵ_θ represents the trained noise predictor U-Net model. We present the complete training and sampling procedures in Algorithms 1 and 2 respectively.

Algorithm 1 Training

```

Input:  $c$ 
repeat
   $x_0 \sim q(x_0)$ 
   $t \sim \text{Uniform}(\{1, \dots, T\})$ 
   $\epsilon \sim \mathcal{N}(0, \mathbf{I})$ 
   $x_t = \sqrt{\bar{\alpha}_t} x_0 + \sqrt{1 - \bar{\alpha}_t} \epsilon$ 
   $\tilde{x}_t = x_t \oplus c$ 
  Take gradient descent step on
   $\nabla_\theta L_{MAE}(\epsilon, \epsilon_\theta(\tilde{x}_t, t))$ 
until converged
  
```

Algorithm 2 Sampling

```

Input:  $c$ 
  sample  $x_T \sim \mathcal{N}(0, \mathbf{I})$ ,  $c$ 
  for  $t = T, \dots, 1$  do
    if  $t > 1$ , then  $z \sim \mathcal{N}(0, \mathbf{I})$ , else  $z = 0$ 
     $\tilde{x}_t = x_t \oplus c$ 
     $\epsilon' = \epsilon_\theta(\tilde{x}_t, t)$ 
     $x_{t-1} = \frac{1}{\sqrt{\alpha_t}} \left( x_t - \frac{1 - \alpha_t}{\sqrt{1 - \bar{\alpha}_t}} \epsilon' \right) + \sigma_t z$ 
  end for
  return  $x_0$ 
  
```

A. Loss Function

Pixel-wise losses such as $L1$ and $L2$ are commonly used in the literature of DDPM papers [22]. In our study, we observed that the $L2$ loss (i.e., $L2 = \mathbb{E}_{t,x_0,\epsilon} [|\epsilon - \epsilon_\theta(x_t, t)|^2]$) resulted in noisier images compared to the $L1$ loss (i.e., $L1 = \mathbb{E}_{t,x_0,\epsilon} [|\epsilon - \epsilon_\theta(x_t, t)|]$). The $L2$ loss function, due to its computation of the squared difference between the estimated value and the target value, is sensitive to outliers. On the other hand, the $L1$ loss calculates the absolute differences between the estimated value and the target value, making it relatively less sensitive to outliers. Hence, in our main experiments, we utilize the $L1$ loss:

$$L_{MAE} = \frac{1}{n} \sum_{i=1}^n |\epsilon_i - \epsilon'_i|, \quad (4)$$

where ϵ_i and ϵ'_i represent the pixels of the original noise added to the input and the predicted noise from the model (i.e., $\epsilon' = \epsilon_\theta(\tilde{x}_\theta, t)$) respectively, n is the total number of pixels ($n = w \cdot h \cdot d$).

III. EXPERIMENTS AND RESULTS

A. Datasets and Image Preprocessing

We used unnormalized clinical brain Magnetic Resonance (MR) images without skull stripping. Our evaluation was performed on the clinical stereotactic radiosurgery dataset [34], which included 1688 contrast-enhanced T1-weighted (T1c) whole-head MR images and corresponding segmentation masks for various brain lesions. The dataset was obtained from patients undergoing Cyberknife radiosurgery at the National Taiwan University Hospital (NTUH). For image preprocessing, we employed MRIProcessor² for image registration and ensured consistent image dimensions by applying cropping and padding. The resulting dimensions were 192x192x192, which were then resized to 128x128x128 with a slice thickness of 1.5x1.5x1.5mm. To improve training data quality, we removed outlier images, performed intensity rescaling, and

²<https://github.com/ReubenDo/MRIProcessor>

normalized the image intensities to the range of [-1,1]. The segmentation mask annotations included three classes: class 0 for the background, class 1 for the head, and class 2 for the tumor area. For evaluation, we created two sub-datasets from the main dataset. The first mode involved a training set of 1292 images and a test set of 208 images. In the second mode, we randomly selected 100 images for training, 100 images for validation, and 100 images for testing, creating a toy dataset.

B. Experiment Details

We evaluated our proposed method in two modes: training with 1,292 images and training with a toy dataset containing only 100 training images. Since there is limited research on mask-to-image medical 3D synthesis, we chose Pix2Pix GAN [35] and DiscoGAN [36] as baseline models and adapted their architecture to 3D models.

In the first mode, we trained our proposed model and the baseline GAN models using 1,292 images for 100,000 epochs with a batch size of 1 (referred to as main models). The evaluation of these models was performed on 208 testing images.

Our Med-DDPM model was trained using the L1 loss, the cosine noise schedule for 250 steps, a learning rate of 10^{-5} for the first 50,000 epochs, and 10^{-6} for the last 50,000 epochs. We used the Adam optimizer with 64 channels in the first layer and employed an attention head at resolution 16. For the Baseline 2 GAN models, Pix2Pix and DiscoGAN, we trained them using a combination loss of Mean Squared Error and L1 Losses, which yielded better results. These models utilized the Adam optimizer with a learning rate of 2×10^{-4} and momentum decays of 0.5 and 0.999.

In the second mode, we trained all models from scratch using the toy dataset for 50,000 epochs with a batch size of 1 (referred to as toy models). Additionally, we employed the toy dataset and synthetic images generated by the toy models to train segmentation models. To assess the effectiveness of synthetic images as a viable alternative to data augmentation, we conducted a comprehensive empirical study. Specifically, we utilized a simple 3D U-Net model [26] for tumor segmentation. The model was trained on various combinations of synthetic data and compared against the performance of the 3D U-Net model trained on real data, as well as augmented images generated using state-of-the-art augmentations from nnU-Net [37]. The segmentation models were trained for 100 epochs using the Binary Cross-Entropy (BCE) loss with a batch size of 4. Model performance was evaluated using the Dice coefficient, IoU, Accuracy, Recall, and Precision scores. All models were trained on Tesla V100-SXM2 32 GB GPU card.

C. Evaluation Metric

We employed quantitative and qualitative measures to evaluate the synthetic images.

Quantitative Evaluation: The Fréchet Inception Distance (FID) [38] is a widely used evaluation metric in GAN synthesis, yet its application in assessing 3D medical images is limited due to its dependency on the Inception-v3 network [39]

trained on a 2D image dataset. Building upon existing research [40], [41], we implemented the 3D-FID metric utilizing a pre-trained 3D Resnet model [42] for feature extraction. However, this approach delivered unsatisfactory measurements. Hence, inspired by the normalization methods found in prior studies [43]–[45], we propose an extended 3D-FID metric incorporating histogram equalization. This adjustment accurately computes image quality distances. Besides the 3D-FID metric, we utilized Mean Squared Error (MSE), Maximum Mean Discrepancy (MMD) score [46], and Multi-Scale Structural Similarity Index Measure (MS-SSIM) [47] for quantitative evaluation.

Qualitative Evaluation: Two approaches were employed for the qualitative evaluation.

First, a visual evaluation was conducted with two neurosurgeons. The experts assessed a set of 40 high-resolution images, comprising an equal mix of 20 real and 20 synthetic images, with the objective of distinguishing them as real or fake. The images evaluated by the experts included samples from both a real image dataset and synthetic images generated by our proposed model. The experts made their classifications based solely on visual assessment. It is important to note that due to the easily identifiable non-realistic features of synthetic images generated by baseline GAN models, we did not proceed with further visual assessment of those GAN synthetic images.

Secondly, the tumor segmentation performance of a 3D U-Net model was evaluated to determine the effectiveness of synthetic images as a data augmentation technique. Various training scenarios were explored using a toy dataset. These scenarios encompassed training exclusively on the toy dataset, incorporating state-of-the-art data augmentations. It is worth noting that all generative models were trained using only 100 images from the toy dataset.

D. Generated Images

Fig. 2 illustrates the coronal, sagittal, and axial slices of real images alongside the generated samples from the proposed method and baseline GAN models. To facilitate a more comprehensive comparison, Fig. 3 presents zoomed-in images of tumor areas in the axial planes of both real and synthetic images. Furthermore, Fig. 4 showcases synthetic images generated using manipulated masks, while Fig. 5 exhibits the diversity of synthetic images generated for a single input mask.

The Pix2Pix baseline model struggles to produce accurate results when generating images from unseen test masks, resulting in blurry images. In contrast, the DiscoGAN model performs better, generating more realistic images with clear tumor areas exhibiting complete ring enhancement and reduced blur compared to the Pix2Pix model. However, it is worth noting that the DiscoGAN generated images fail to clearly depict the distinctive features of the brain. Additionally, they generate coarse gyri and sulci, which appear unnatural.

In contrast, the proposed Med-DDPM model generates highly realistic and high-quality images, exhibiting clear visibility of both brain features and tumor regions. Although DDPM often generates incomplete ring enhancement of the tumors, this phenomenon is also present in the real images.

TABLE I
QUANTITATIVE RESULTS

| Method | MSE↓ | MMD↓ | 3D-FID↓ | MS-SSIM |
|-----------------|---------------|---------------|------------------|---------------|
| DiscoGAN | 0.0554±0.0001 | 4.7598±2.3593 | 257.1587±0.0588 | 0.4342±0.0009 |
| Pix2Pix | 0.0668±7.4882 | 6.0538±1.3325 | 307.1682±19.9522 | 0.3032±0.0003 |
| Med-DDPM (Ours) | 0.0548±0.0001 | 4.1909±2.6069 | 249.713±17.9522 | 0.4358±0.0010 |
| Real | - | - | - | 0.4728±0.0013 |

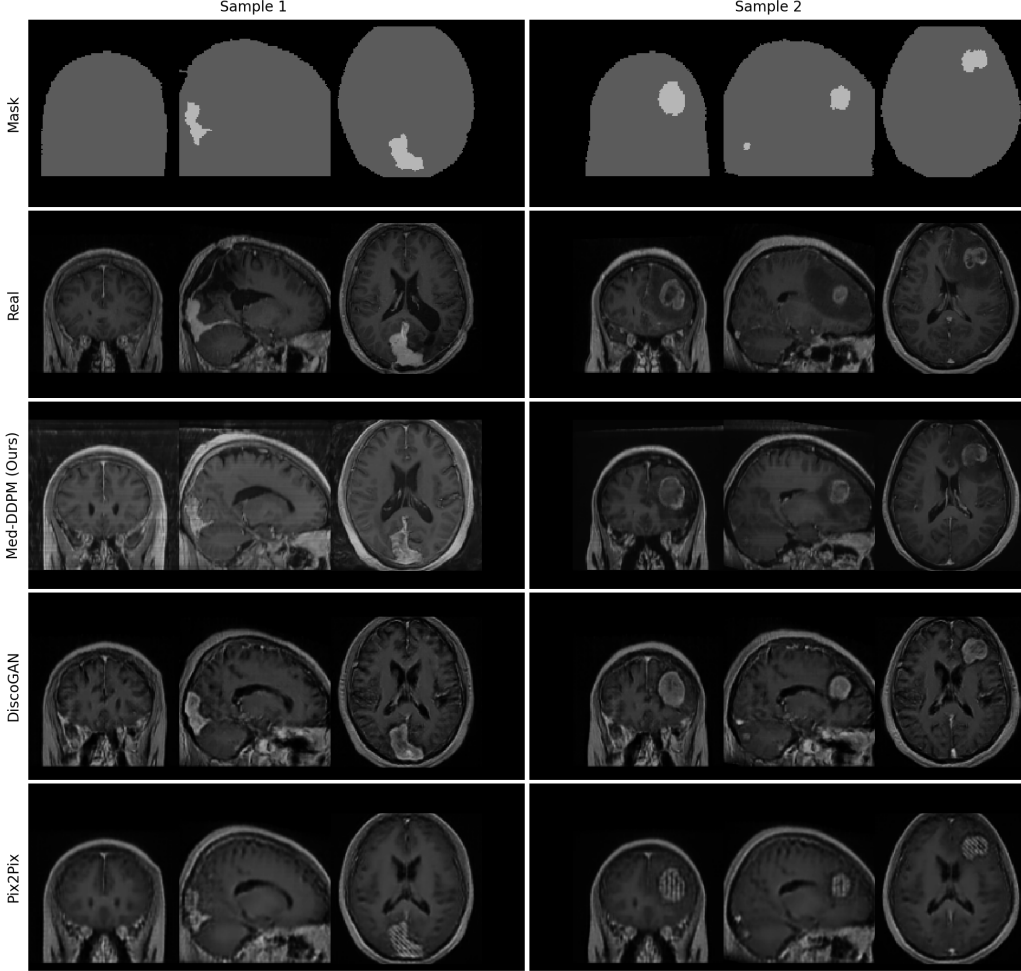


Fig. 2. Comparison of real and synthetic samples in coronal, sagittal, and axial slices. The synthetic samples generated by DiscoGAN exhibit realistic tumor areas, similar to our proposed method. However, the brain part of DiscoGAN appears coarse and cannot be compared to Med-DDPM. Pix2pix produces poor image results.

Furthermore, the peri-tumoral edema generated by DDPM is more realistic, compared to the neatly isotropic low intensity generated by DiscoGAN. These synthesized images bear a much closer resemblance to the real images, accurately capturing intricate details.

1) *Quantitative results:* The comprehensive quantitative evaluation of the competing methods is summarized in Table I, which highlights the performance of the proposed model, Med-DDPM, in comparison to the established baselines, DiscoGAN and Pix2Pix. The models were assessed based on four critical metrics: Mean Squared Error (MSE), Maximum Mean Discrepancy (MMD), Multi-Scale Structural Similarity Index (MS-SSIM), and the proposed 3D Fréchet Inception Distance (3D-FID).

A detailed analysis of the results demonstrates the superior

performance of Med-DDPM. It achieved the lowest MSE of 0.0548, indicating its robust capability to preserve finer details and structures in the output. Furthermore, Med-DDPM outperformed in terms of MMD, with a value of 4.1909, suggesting its strong ability to match the distribution of the target domain.

Examination of the 3D-FID values for the Med-DDPM model revealed significantly lower scores, with a value of 249.713. This result highlighted the proficiency of Med-DDPM in generating realistic and high-quality 3D structures. Although the MS-SSIM score of the model (0.4358) was not as close to the MS-SSIM score of the real data (0.4728), it positioned the model closer to the real data when compared to Pix2Pix. Furthermore, the MS-SSIM score of DiscoGAN was also comparable, with a score of 0.4342, indicating the

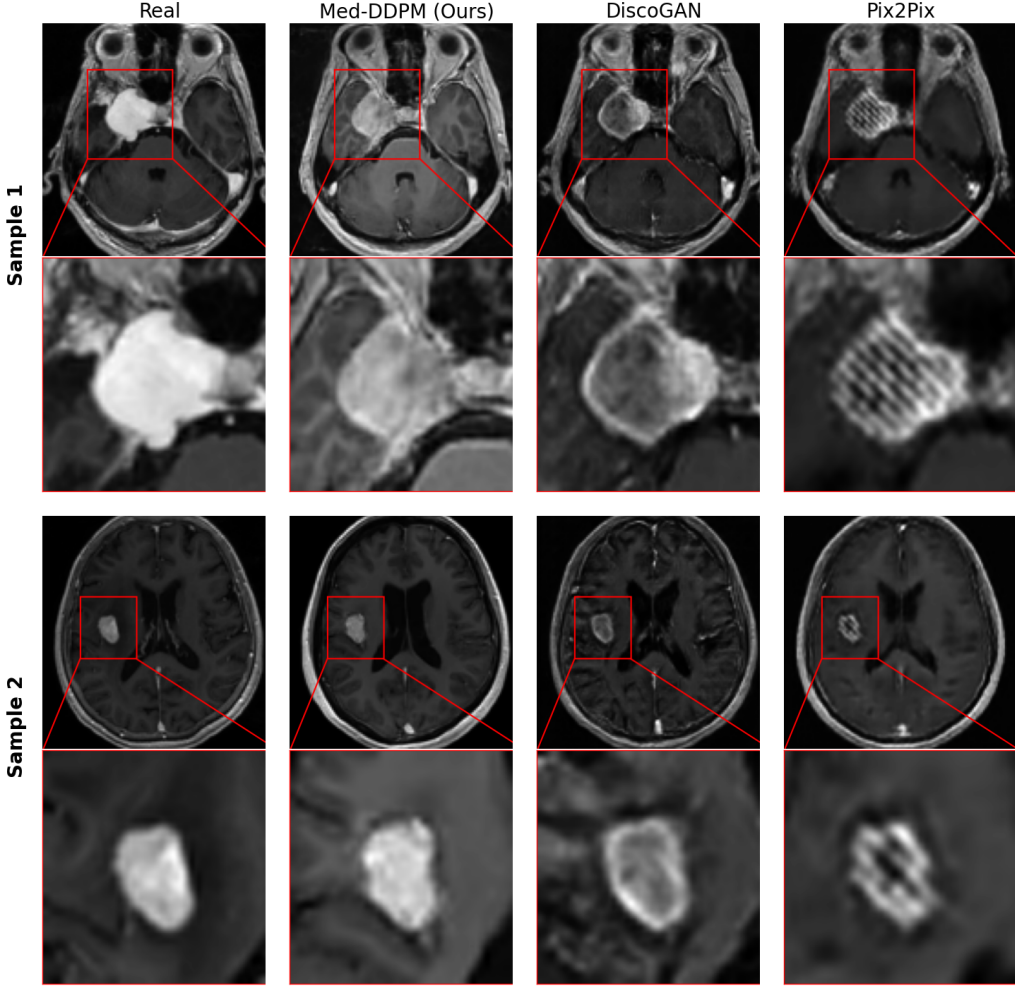


Fig. 3. Zoomed visual comparison of tumor areas in real and generated samples (axial view slices). Med-DDPM and DiscoGAN generate more realistic tumor parts with smoother edges and less artifacts. Pix2Pix, on the other hand, has poor tumor synthesis, with strong artifacts that look unrealistic.

potential for further improvement in the model to match the MS-SSIM score of the real data.

It is important to note that while Med-DDPM excelled in most metrics, DiscoGAN demonstrated comparable performance in terms of MSE and MS-SSIM. Nevertheless, when considering all evaluation metrics collectively, Med-DDPM outperformed the baseline models.

2) Qualitative results: Regular visual assessment tests were conducted throughout the experimentation phase. The experts were presented with a mixture of real and synthetic 3D images generated by the proposed model and the two baseline models. The experts evaluated the quality of the generated images. It was evident to the experts that the synthetic images produced by the two baseline models exhibited blurriness and lacked realistic-looking brain features. In contrast, the synthetic images generated by our proposed method appeared more realistic. However, upon careful examination of the axial plane, the experts were able to identify the synthetic images due to slight inconsistencies in vessel continuity within the Circle of Willis area. Additionally, the synthetic images did not exhibit the presence of mass effects around large tumors, which typically result in shifts in the ventricles and the midline

(as shown in the axial slice of real image sample 2 in Fig. 2).

Furthermore, we conducted an additional experiment aimed at assessing slice-wise 2D images, specifically center-cut slices of both real and synthetic samples generated using our proposed method. In this experiment, the experts encountered challenges in distinguishing between the real and synthetic images, as they were unable to differentiate the synthetic images from the real ones.

E. Comparison of Segmentation Models Trained on Synthetic Images

The results from the experiments conducted using synthetic and real images to train U-Net for tumor segmentation on the toy dataset are presented in Table II. The synthetic images are generated using different methods, including the proposed Med-DDPM toy model, trained on 100 images from the toy dataset, as well as two GAN models (DiscoGAN and Pix2Pix) trained on the same dataset. Additionally, state-of-the-art augmentations were applied to manipulate the 100 training images from the toy dataset.

Using the training set from the toy dataset as a baseline, the average Dice score, IoU, Accuracy, Recall, and Precision

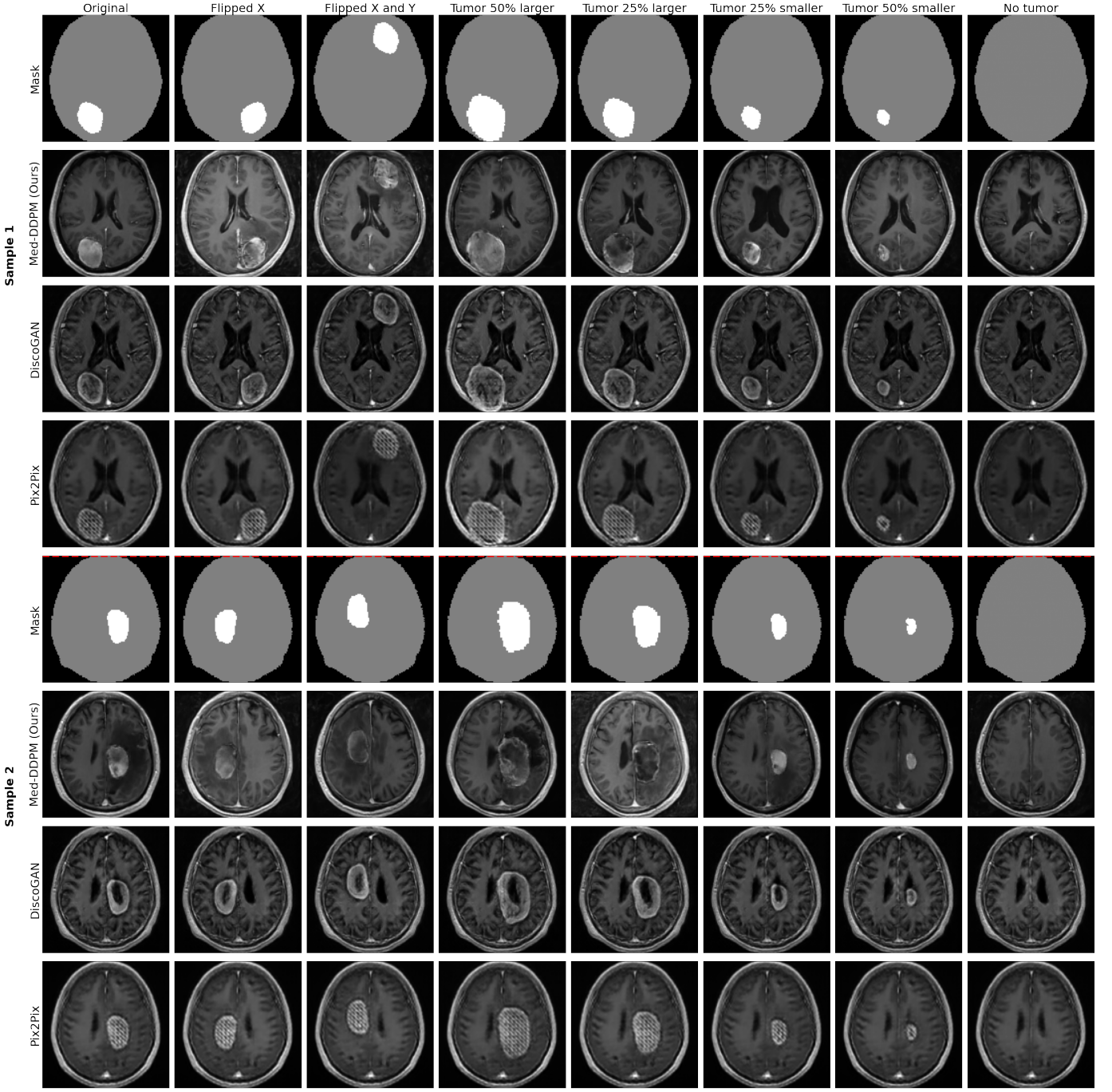


Fig. 4. Comparison of synthetic images generated with manipulated masks (axial view slices). DiscoGAN primarily captures the same brain features, with only slight variations in pixel intensities for tumor parts. Pix2Pix also exhibits a similar limitation, highlighting the issue of mode collapse and the lack of diverse image generation in GAN models. In contrast, the proposed method, Med-DDPM, excels in synthesizing diverse images with strong variations.

are 0.2805, 0.2125, 0.2493, 0.2493, and 0.5100, respectively. Training with synthetic images, except for Pix2Pix model, consistently outperforms the baseline of real images.

Synthetic images generated through state-of-the-art augmentations consistently achieve the highest performance. With 1000, 2000, and 5000 images, the Dice score increases to 0.4442, 0.4688, and 0.4704 respectively, representing significant improvements. IoU also sees considerable increases to 0.3509, 0.3745, and 0.3796 for the same set sizes. This improvement is likely due to the fact that the augmented

images are derived from manipulations of real training images, capturing the intricate and relevant features of real tumor images while increasing the diversity of the training data. The proposed method, Med-DDPM, provides a remarkable improvement over the baseline and other GAN models (Fig. 6), with Dice scores of 0.3593, 0.3746, and 0.3563 for the 1000, 2000, and 5000 images sets respectively. This improvement signifies that the Med-DDPM method captures the intricacies of the segmentation task better than the other GAN models and is much closer to the performance achieved by the state-

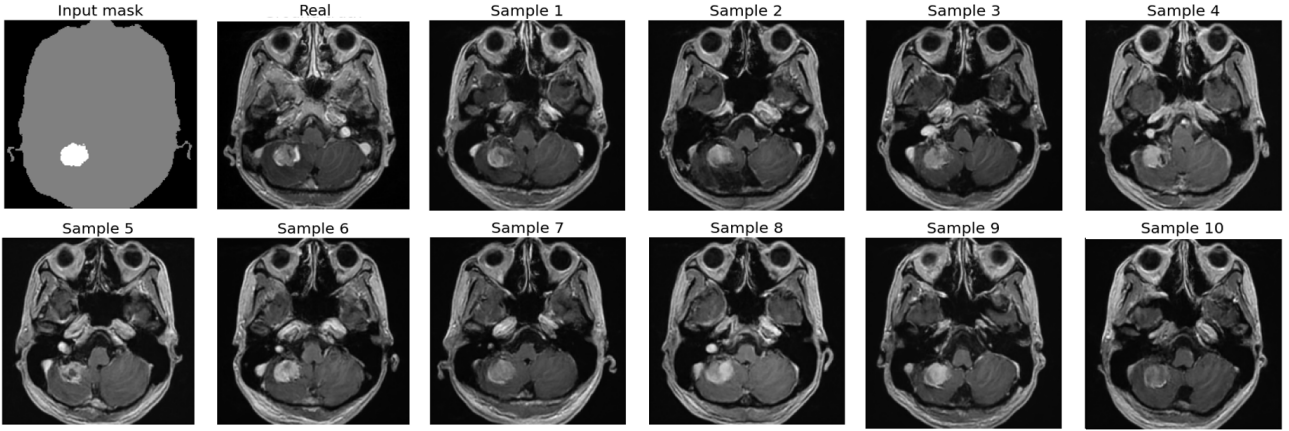


Fig. 5. Center-cut axial slices of generated samples, showcasing the output diversity of Med-DDPM for a single input mask.

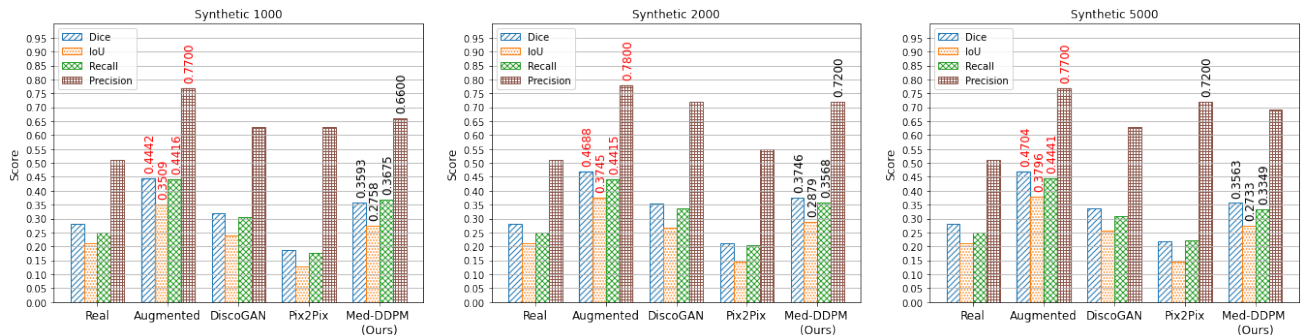


Fig. 6. Visual comparison of segmentation model results for different methods, including the baseline results for real images and state-of-the-art augmentations. Augmentation results are represented with label values in red, while the highest values of each method are highlighted in black.

TABLE II
PERFORMANCE SUMMARY OF SEGMENTATION MODELS TRAINED ON SYNTHETIC IMAGES

| Experiment | Method | Dice | IoU | Accuracy | Recall | Precision |
|------------|--------------------------------------|----------------------|----------------------|----------------------|----------------------|----------------------|
| - | Real images | 0.2805±0.3218 | 0.2125±0.2613 | 0.2493±0.3125 | 0.2493±0.3125 | 0.5100±0.4998 |
| Syn 1000 | Augmented images | 0.4442±0.3422 | 0.3509±0.2958 | 0.4416±0.3702 | 0.4416±0.3702 | 0.7700±0.4208 |
| | DiscoGAN | 0.3177±0.3197 | 0.2387±0.2616 | 0.3062±0.3304 | 0.3062±0.3304 | 0.6300±0.4828 |
| | Pix2Pix | 0.1870±0.2375 | 0.1264±0.1756 | 0.1759±0.2327 | 0.1759±0.2327 | 0.6300±0.4828 |
| | Med-DDPM (Ours) | 0.3593±0.3334 | 0.2758±0.2781 | 0.3675±0.3606 | 0.3675±0.3606 | 0.6600±0.4737 |
| | Med-DDPM + DiscoGAN | 0.3762±0.3523 | 0.2969±0.2992 | 0.3550±0.3552 | 0.3550±0.3552 | 0.6400±0.4800 |
| | Med-DDPM + Pix2Pix | 0.3056±0.3372 | 0.2362±0.2769 | 0.2561±0.3022 | 0.2561±0.3022 | 0.5800±0.4936 |
| | DiscoGAN + Pix2Pix | 0.3405±0.3222 | 0.2566±0.2642 | 0.3006±0.3029 | 0.3006±0.3029 | 0.6800±0.4665 |
| Syn 2000 | Augmented images | 0.4688±0.3436 | 0.3745±0.3030 | 0.4415±0.3551 | 0.4415±0.3551 | 0.7800±0.4142 |
| | DiscoGAN | 0.3558±0.3143 | 0.2658±0.2575 | 0.3356±0.3208 | 0.3356±0.3208 | 0.7200±0.4490 |
| | Pix2Pix | 0.2122±0.2593 | 0.1467±0.1911 | 0.2032±0.2512 | 0.2032±0.2512 | 0.5500±0.4974 |
| | Med-DDPM (Ours) | 0.3746±0.3311 | 0.2879±0.2798 | 0.3568±0.3426 | 0.3568±0.3426 | 0.7200±0.4490 |
| | Med-DDPM + DiscoGAN | 0.4389±0.3340 | 0.3417±0.2824 | 0.4225±0.3404 | 0.4225±0.3404 | 0.7500±0.4330 |
| | Med-DDPM + Pix2Pix | 0.3346±0.3284 | 0.2549±0.2709 | 0.2772±0.2929 | 0.2772±0.2929 | 0.6600±0.4737 |
| | DiscoGAN + Pix2Pix | 0.3441±0.3371 | 0.2650±0.2792 | 0.3027±0.3154 | 0.3027±0.3154 | 0.6300±0.4828 |
| Syn 5000 | Med-DDPM + DiscoGAN + Pix2Pix | 0.4436±0.3533 | 0.3537±0.3014 | 0.4485±0.3739 | 0.4485±0.3739 | 0.7300±0.4440 |
| | Augmented images | 0.4704±0.3545 | 0.3796±0.3095 | 0.4441±0.3569 | 0.4441±0.3569 | 0.7700±0.4208 |
| | DiscoGAN | 0.3379±0.3313 | 0.2578±0.2724 | 0.3091±0.3291 | 0.3091±0.3291 | 0.6300±0.4828 |
| | Pix2Pix | 0.2170±0.2366 | 0.1447±0.1721 | 0.2206±0.2539 | 0.2206±0.2539 | 0.7200±0.4490 |
| | Med-DDPM (Ours) | 0.3563±0.3311 | 0.2733±0.2782 | 0.3349±0.3341 | 0.3349±0.3341 | 0.6900±0.4624 |
| | Med-DDPM + DiscoGAN | 0.4236±0.3363 | 0.3298±0.2843 | 0.3837±0.3266 | 0.3837±0.3266 | 0.7300±0.4440 |
| | Med-DDPM + Pix2Pix | 0.3823±0.3094 | 0.2856±0.2551 | 0.3229±0.2862 | 0.3229±0.2862 | 0.7800±0.4142 |

The results of evaluating a segmentation model trained exclusively on synthetic images. The synthetic images used for training were generated from toy models that were solely trained using the training set of the toy dataset, comprising 100 images. To enable a comparison of augmentation methods, augmented images were created by applying state-of-the-art augmentations of nnU-Net to manipulate the training images from the toy dataset. The evaluation scores represent the performance of the segmentation model on the test set, which consists of 100 images from the toy dataset. The term "Real images" refers to the 100 training images from the toy dataset and serves as the baseline for comparison. Syn 1000, Syn 2000, and Syn 5000 indicate the number of synthetic images used in training the segmentation model. Comparing the results of state-of-the-art augmentations, the best outcomes are highlighted in bold.

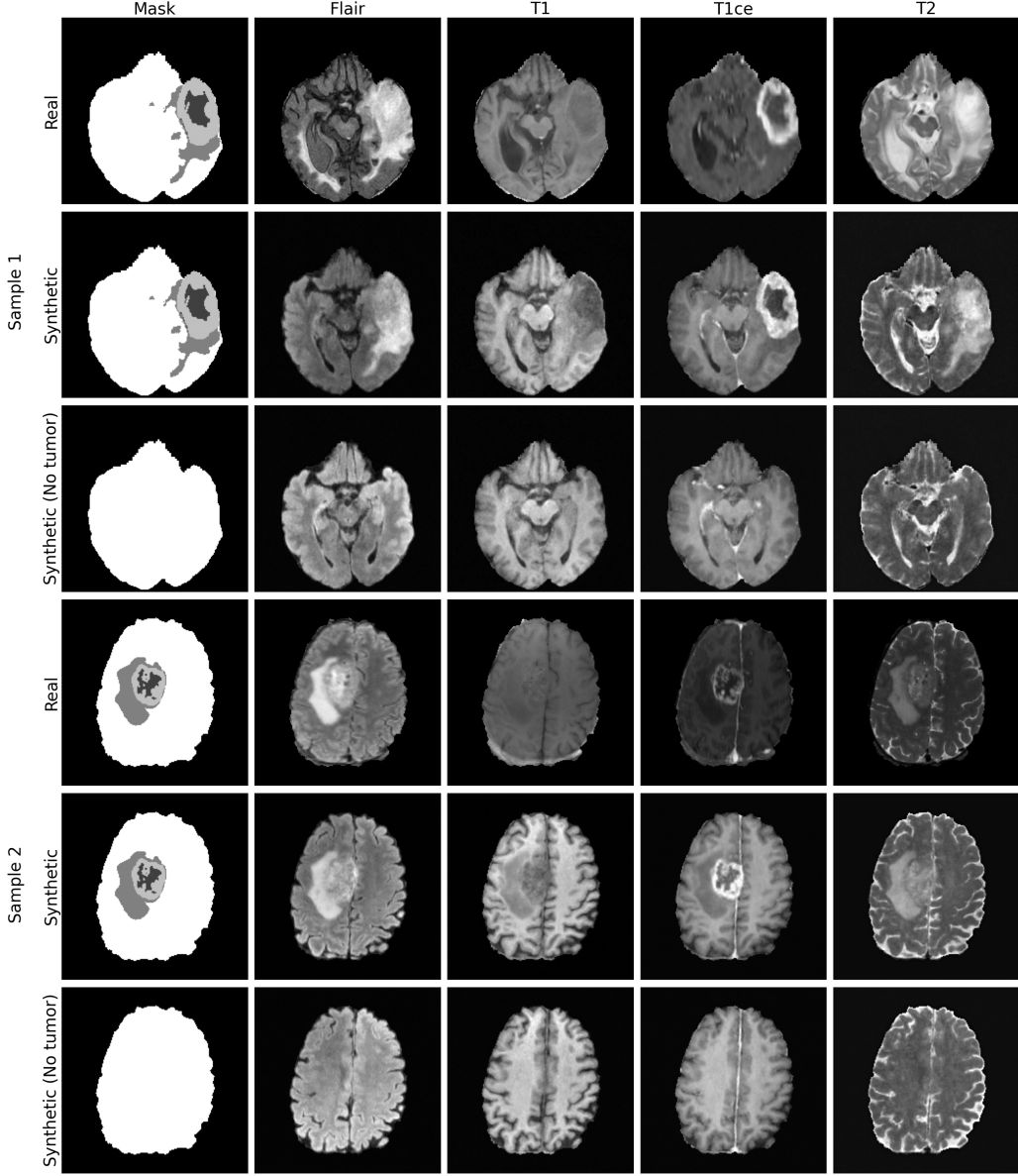


Fig. 7. Axial view comparison of real and generated images in the 4 modalities synthesis experiment (Largest tumor slice)

of-the-art augmentations.

Interestingly, when Med-DDPM is combined with DiscoGAN and Pix2Pix, the results become even more promising, suggesting that these methods complement each other in generating effective synthetic images for tumor segmentation. Particularly in the experiment with 5000 synthetic images, Med-DDPM in combination with DiscoGAN and Pix2Pix achieves a Dice score of 0.4443 and an IoU of 0.3511, which is nearly as good as the state-of-the-art augmentations, demonstrating the potential of Med-DDPM in generating high-quality synthetic images.

Overall, these results illustrate the effectiveness of using synthetic images in training U-Net for tumor segmentation, with the proposed method Med-DDPM, particularly when combined with DiscoGAN and Pix2Pix, demonstrating competitive performance to the state-of-the-art augmentations.

F. 3D Multimodal MRI Synthesis Experiment

In this section, we present the results of an additional experiment conducted to validate the effectiveness of our proposed method, Med-DDPM, for multimodal MRI synthesis. We utilized the brain-extracted MRI dataset from the BraTS2021 challenge³ for this experiment, with the objective of demonstrating the capability of our method in generating high-quality images for all four MRI modalities (T1, T1CE, T2, and Flair) simultaneously from a segmentation mask.

To enhance model training efficiency, we selected 193 high-quality images of all modalities from the dataset and preprocessed them by applying cropping and padding to a size of 192x192x144. The original labels of the segmentation mask in this dataset are 0, 1, 2, and 4, where 1, 2, and 4 represent tumor parts. For better adaptation to our needs, we modified the mask labels as follows: we changed mask labels from 4 to 3

³<http://braintumorsegmentation.org/>

and introduced one more label (label 4) to represent the brain area, achieved by thresholding the T1 image. Consequently, the final class labels were defined as follows: 0 represents the background, 1 to 3 correspond to the tumor parts, and 4 indicates the brain area.

Next, we performed a one-hot encoding operation, excluding the background class label 0. This operation resulted in a mask image with four channels, each representing one of the classes. During the training process, we applied channel-wise concatenation to combine the input training image (including all four modalities T1, T1CE, T2, and Flair concatenated together, resulting in a four-channel image) with the final mask image, also a four-channel image. The resulting concatenated image contains eight channels, and this configuration was used in the training process. For the Med-DDPM model in this experiment, we used the same experimental setups as in our main model training, except we employed 200,000 epochs for this experiment. Due to the high resolution nature of the eight-channel image, we trained our model on the NVIDIA A100 80GB GPU card.

Fig. 7 illustrates a comparison between the generated samples from our experiment and the corresponding real images. The images generated by our proposed method exhibit a high level of fidelity and closely resemble the actual MRI modalities. This outcome further highlights the robustness and accuracy of our approach in effectively generating multiple modalities from a single segmentation mask.

IV. DISCUSSION

In the present study, we introduced Med-DDPM, a groundbreaking approach for synthesizing high-quality, diverse 3D medical images using a conditional denoising diffusion probabilistic model. Our model incorporated a conditioning mask image as a prior in both the training and sampling stages. The results confirmed the superiority of Med-DDPM in generating 3D medical images that were not only of high quality but also encompassed a wide range of variability.

When compared to established baseline GAN models, DiscoGAN and Pix2Pix, Med-DDPM exhibited remarkable capabilities, especially in accurately synthesizing brain lesion regions and capturing intricate features. However, we also identified certain limitations of Med-DDPM through our analysis. Specifically, slight inconsistencies were observed in vessel continuity within the Circle of Willis area of the brain. While our synthetic images appeared realistic, experts could discern these inconsistencies and differentiate them from real MR images. Additionally, although Med-DDPM outperformed the GAN models in terms of overall image realism, DiscoGAN showed potential in forming complete rings around tumor shapes.

The experiments conducted with segmentation models trained on synthetic images generated by Med-DDPM demonstrated a substantial improvement in segmentation performance. This success underscores the potential of Med-DDPM as a powerful tool for data augmentation in medical imaging and as an advanced data anonymization tool in the medical imaging domain. This could help address data sharing challenges across different institutions and facilitate the further

development of AI in medical imaging without being hindered by privacy concerns.

However, despite these promising results, Med-DDPM did not entirely match the performance of state-of-the-art augmentation techniques that involve manipulating real training images. This emphasizes the current limitations of synthetic images and the scope for further enhancement in our model.

V. CONCLUSION

In summary, this study confirms the potential of Med-DDPM as an innovative and effective solution for 3D medical image synthesis. Despite certain limitations, Med-DDPM consistently demonstrated superior results compared to traditional GAN-based models, particularly in preserving finer details and structures and matching the distribution of the target domain. The utilization of Med-DDPM synthetic images alone significantly enhanced segmentation performance, and the combination of synthetic images from GAN models further improved segmentation performance, bringing it closer to state-of-the-art augmentations. This showcases the potential of the proposed method as a data augmentation and medical image anonymization tool.

Med-DDPM represents a significant advancement in addressing challenges related to data scarcity, class imbalance, and privacy concerns in the field of medical imaging. Future work will focus on enhancing the current model, potentially through the integration of latent diffusion models to enhance its image generation capabilities. These developments are expected to bring us closer to our ultimate goal of leveraging synthetic images to improve data augmentation and comprehensive anonymization, and driving progress in the field of medical imaging.

As we continuously improve upon Med-DDPM, we eagerly anticipate delivering high-quality and anatomically coherent images, tackling challenges associated with data scarcity and privacy concerns, and advancing the application of AI in the healthcare sector.

ACKNOWLEDGMENT

This work was supported by the National Science and Technology Council, Taiwan [Grant No. 111-2221-E-002-049-MY3] and National Taiwan University Hospital [Grant No. 110-EDN03].

REFERENCES

- [1] M. Puttagunta and S. Ravi, "Medical image analysis based on deep learning approach," *Multimedia Tools and Applications*, vol. 80, no. 16, pp. 24365-24398, Jul. 2021. doi: 10.1007/s11042-021-10707-4.
- [2] G. Litjens *et al.*, "A survey on deep learning in medical image analysis," *Medical Image Analysis*, vol. 42, pp. 60-88, 2017. doi: 10.1016/j.media.2017.07.005.
- [3] K. He *et al.*, "Transformers in Medical Image Analysis: A Review," *Intelligent Medicine*, vol. 2022, 2022. doi: 10.1016/j.imed.2022.07.002.
- [4] A. R. Luca, T. F. Ursuleanu, L. Gheorghe, R. Grigorovici, S. Iancu, M. Hluscneac, A. Grigorovici, "Impact of quality, type and volume of data used by deep learning models in the analysis of medical images," *Informatics in Medicine Unlocked*, vol. 29, pp. 100911, 2022. doi: 10.1016/j.imu.2022.100911.
- [5] M. H. Hesamian, W. Jia, X. He, and P. Kennedy, "Deep Learning Techniques for Medical Image Segmentation: Achievements and Challenges," *J Digit Imaging*, vol. 32, no. 4, pp. 582-596, Aug. 2019. doi: 10.1007/s10278-018-0159-6.

- [6] L. M. Prevedello *et al.*, "Challenges Related to Artificial Intelligence Research in Medical Imaging and the Importance of Image Analysis Competitions," *Radiology: Artificial Intelligence*, vol. 1, no. 1, p. e180031, 2019. doi: 10.1148/ryai.2019180031.
- [7] Z. Li, K. Kamnitsas, and B. Glocker, "Overfitting of Neural Nets Under Class Imbalance: Analysis and Improvements for Segmentation," in *Medical Image Computing and Computer Assisted Intervention – MICCAI 2019*, D. Shen *et al.* (Eds.), Cham: Springer International Publishing, 2019, pp. 402–410, ISBN: 978-3-030-32248-9.
- [8] A. Zhang, L. Xing, J. Zou, and J. C. Wu, "Shifting machine learning for healthcare from development to deployment and from models to data," *Nature Biomedical Engineering*, vol. 6, no. 12, pp. 1330–1345, 2022. doi: 10.1038/s41551-022-00898-y.
- [9] H.-C. Shin *et al.*, "Medical image synthesis for data augmentation and anonymization using generative adversarial networks," in *Simulation and Synthesis in Medical Imaging*, 1st ed., vol. 11037, M. A. Horsch *et al.* (Eds.), Springer, 2018, pp. 1–11. ISBN: 978-3-030-00536-8, doi: 10.1007/978-3-030-00536-8-1.
- [10] X. Yi, E. Walia, and P. Babyn, "Generative adversarial network in medical imaging: A review," *Medical Image Analysis*, vol. 58, p. 101552, 2019. doi: <https://doi.org/10.1016/j.media.2019.101552>.
- [11] Y. Chen *et al.*, "Generative Adversarial Networks in Medical Image augmentation: A review," *Computers in Biology and Medicine*, vol. 144, p. 105382, 2022. doi: <https://doi.org/10.1016/j.combiomed.2022.105382>.
- [12] E. Ahishakiye, M. B. Van Gijzen, J. Tumwiine, R. Wario, and J. Obungoloch, "A survey on deep learning in medical image reconstruction," *Intelligent Medicine*, vol. 1, no. 3, pp. 118–127, 2021. doi: <https://doi.org/10.1016/j.imed.2021.03.003>.
- [13] B. K. Beaulieu-Jones *et al.*, "Privacy-Preserving Generative Deep Neural Networks Support Clinical Data Sharing," *Circulation: Cardiovascular Quality and Outcomes*, vol. 12, e005122, 2019, doi: <https://doi.org/10.1161/CIRCOUTCOMES.118.005122>.
- [14] J. Yoon, L. N. Drumright, and M. van der Schaar, "Anonymization Through Data Synthesis Using Generative Adversarial Networks (ADS-GAN)," *IEEE Journal of Biomedical and Health Informatics*, vol. 24, no. 8, pp. 2378–2388, 2020. doi: 10.1109/jbhi.2020.2980262. PMID: 32167919.
- [15] Y. Al Khalil, S. Amirrajab, C. Lorenz, J. Weese, J. Pluim, and M. Breeuwer, "On the usability of synthetic data for improving the robustness of deep learning-based segmentation of cardiac magnetic resonance images," in *Medical Image Analysis*, vol. 84, p. 102688, 2023. doi: <https://doi.org/10.1016/j.media.2022.102688>.
- [16] V. Fernandez *et al.*, "Can Segmentation Models Be Trained with Fully Synthetically Generated Data?," in *Zhao, C., Svoboda, D., Wolterink, J.M., Escobar, M. (eds) Simulation and Synthesis in Medical Imaging. SASHIMI 2022. Lecture Notes in Computer Science*, vol 13570, Springer, Cham, 2022.
- [17] A. B. Qasim *et al.*, "Red-GAN: Attacking class imbalance via conditioned generation. Yet another medical imaging perspective," in *Proceedings of the Third Conference on Medical Imaging with Deep Learning*, vol. 121, 2020, pp. 655–668. [Online]. Available: <https://proceedings.mlr.press/v121/qasim20a.html>
- [18] D. Saxena, and J. Cao, "Generative Adversarial Networks (GANs): Challenges, Solutions, and Future Directions," in *ACM Comput. Surv.*, vol. 54, no. 3, Art. no. 63, April 2022, pp. 1–42, doi: 10.1145/3446374.
- [19] Y. Skandarani, P.-M. Jodoin, and A. Lalonde, "GANs for Medical Image Synthesis: An Empirical Study," in *Journal of Imaging*, vol. 9, no. 3, 2023, p. 69. [Online]. Available: <https://www.mdpi.com/2313-433X/9/3/69>.
- [20] L. Wang, W. Chen, W. Yang, F. Bi, and F. R. Yu, "A State-of-the-Art Review on Image Synthesis With Generative Adversarial Networks," in *IEEE Access*, vol. 8, 2020, pp. 63514–63537, doi: 10.1109/ACCESS.2020.2982224.
- [21] D. Prafulla and N. Alexander, "Diffusion Models Beat GANs on Image Synthesis," *Adv. Neural Inf. Process Syst.*, vol. 34, 2021.
- [22] L. Yang *et al.*, "Diffusion Models: A Comprehensive Survey of Methods and Applications," arXiv preprint arXiv:2209.00796, 2023.
- [23] A. Kazerouni *et al.*, "Diffusion models in medical imaging: A comprehensive survey," in *Medical Image Analysis*, vol. 88, 2023, p. 102846, doi: <https://doi.org/10.1016/j.media.2023.102846>.
- [24] Z. Dorjsembe, S. Odonchimed, and F. Xiao, "Three-Dimensional Medical Image Synthesis with Denoising Diffusion Probabilistic Models," in *Medical Imaging with Deep Learning*, 2022.
- [25] J. Ho, A. Jain, and P. Abbeel, "Denoising Diffusion Probabilistic Models," arXiv preprint arXiv:2006.11239, 2020.
- [26] Ö. Çiçek, A. Abdulkadir, S. S. Lienkamp, T. Brox, and O. Ronneberger, "3D U-Net: Learning Dense Volumetric Segmentation from Sparse Annotation," in *Medical Image Computing and Computer-Assisted Intervention – MICCAI 2016*, Springer, Cham, 2016, pp. 424–432.
- [27] F.-A. Croitoru *et al.*, "Diffusion Models in Vision: A Survey," *ArXiv*, abs/2209.04747, 2022.
- [28] Z. Xiao, K. Kreis, and A. Vahdat, "Tackling the Generative Learning Trilemma with Denoising Diffusion GANs," in *International Conference on Learning Representations*, 2022, URL: <https://openreview.net/forum?id=JprM0p-q0Co>.
- [29] F. Khader *et al.*, "Denoising diffusion probabilistic models for 3D medical image generation," *Scientific Reports*, vol. 13, no. 7303, 2023, doi: 10.1038/s41598-023-34341-2.
- [30] H. Ali, S. Murad, and Z. Shah, "Spot the Fake Lungs: Generating Synthetic Medical Images Using Neural Diffusion Models," in *L. Longo and R. O'Reilly (eds) Artificial Intelligence and Cognitive Science. AICS 2022. Communications in Computer and Information Science*, vol 1662, Springer, Cham, 2023.
- [31] L. X. Nguyen, P. Sone Aung, H. Q. Le, S. -B. Park, and C. S. Hong, "A New Chapter for Medical Image Generation: The Stable Diffusion Method," in *Proceedings of the 2023 International Conference on Information Networking (ICOIN)*, Bangkok, Thailand, 2023, pp. 483–486, doi: 10.1109/ICOIN56518.2023.10049010.
- [32] A. Kazerouni *et al.*, "Diffusion models in medical imaging: A comprehensive survey," in *Medical Image Analysis*, vol. 88, 2023, p. 102846, doi: <https://doi.org/10.1016/j.media.2023.102846>.
- [33] A. Nichol and P. Dhariwal, "Improved Denoising Diffusion Probabilistic Models," *ArXiv*, 2021.
- [34] Wu, Siangruei *et al.*, "Deep Learning-Based Segmentation of Various Brain Lesions for Radiosurgery," *Applied Sciences*, vol. 11, no. 19, article no. 9180, 2021, DOI: 10.3390/app11199180.
- [35] P. Isola *et al.*, "Image-to-Image Translation with Conditional Adversarial Networks," *CoRR*, vol. abs/1611.07004, 2016.
- [36] T. Kim, M. Cha, H. Kim, J. K. Lee, and J. Kim, "Learning to Discover Cross-Domain Relations with Generative Adversarial Networks," in *Proceedings of the 34th International Conference on Machine Learning - Volume 70*, Sydney, NSW, Australia, 2017, pp. 1857–1865.
- [37] F. Isensee *et al.*, "nnU-Net: a self-configuring method for deep learning-based biomedical image segmentation," in *Nat Methods*, vol. 18, pp. 203–211, 2021. <https://doi.org/10.1038/s41592-020-01008-z>.
- [38] M. Heusel, H. Ramsauer, T. Unterthiner, B. Nessler, and S. Hochreiter, "GANs Trained by a Two Time-Scale Update Rule Converge to a Local Nash Equilibrium," *Proceedings of the 31st International Conference on Neural Information Processing Systems*, pp. 6629–6640, 2017, ISBN: 9781510860964.
- [39] C. Szegedy, V. Vanhoucke, S. Ioffe, J. Shlens, and Z. Wojna, "Rethinking the Inception Architecture for Computer Vision," in *2016 IEEE Conference on Computer Vision and Pattern Recognition (CVPR)*, pp. 2818–2826, 2016, doi: 10.1109/CVPR.2016.308.
- [40] P. Subramaniam *et al.*, "Generating 3D TOF-MRA volumes and segmentation labels using generative adversarial networks," *Medical Image Analysis*, vol. 78, pp. 102396, 2022, doi: <https://doi.org/10.1016/j.media.2022.102396>.
- [41] L. Sun, J. Chen, Y. Xu, M. Gong, K. Yu, and K. Batmanghelich, "Hierarchical Amortized GAN for 3D High Resolution Medical Image Synthesis," *IEEE Journal of Biomedical and Health Informatics*, vol. 26, no. 8, pp. 3966–3975, 2022, doi: 10.1109/JBHI.2022.3172976.
- [42] S. Chen, K. Ma, and Y. Zheng, "Med3D: Transfer Learning for 3D Medical Image Analysis," *CoRR*, vol. abs/1904.00625, 2019, arXiv:1904.00625.
- [43] S. Pasha, P. Babu, and Z. Vakil, "Enhancement of MRI Brain Images with Histogram Equalization Techniques," in *Proceedings of the IEEE International Conference on Electrical Sciences and Engineering*, 2019, pp. 1–4, doi: 10.1109/ICESE46178.2019.9194629.
- [44] G. Modanwal, A. Vellal, and M. Mazurowski, "Normalization of Breast MRIs using Cycle-Consistent Generative Adversarial Networks," *Computer Methods and Programs in Biomedicine*, vol. 208, pp. 106225, Jun. 2021, doi: 10.1016/j.cmpb.2021.106225.
- [45] X. Sun *et al.*, "Histogram-based normalization technique on human brain magnetic resonance images from different acquisitions," *BioMedical Engineering OnLine*, vol. 14, no. 1, p. 73, Jul. 28, 2015.
- [46] A. Gretton, K. M. Borgwardt, M. J. Rasch, B. Schölkopf, and A. Smola, "A Kernel Two-Sample Test," *Journal of Machine Learning Research*, vol. 13, no. 25, pp. 723–773, 2012, url: <http://jmlr.org/papers/v13/gretton12a.html>.
- [47] Z. Wang, E.P. Simoncelli, and A.C. Bovik, "Multiscale structural similarity for image quality assessment," in *Proc. The Thirty-Seventh Asilomar Conference on Signals, Systems & Computers, 2003*, vol. 2, pp. 1398–1402, 2003, doi: 10.1109/ACSSC.2003.1292216.